Term Project Report:
Structural Sizing of an Aircraft Wing Structure

Muhammad Alfiyandy Hariansyah (ID: 21023691)
Xi Chen (ID: 21147100)

MECH5930 – Finite Element Methods

December 9, 2025

1 Introduction

1.1 Background and Motivation

An aircraft wing is a primary lifting surface, and its design is fundamental to performance. The trend toward high-aspect-ratio wings, aimed at reducing induced drag, results in structures that are lighter and more flexible. The internal wing structure, which must withstand aerodynamic loads, its own weight, and other operational forces, is therefore critical. As illustrated in Fig. 1, a typical fixed-wing structure consists of spars, ribs, stringers, and the skin. Spars are the main load-bearing members resisting bending and shear, ribs maintain the airfoil shape and transfer loads from the skin to the spars, and the skin, reinforced by stringers, carries torsion and transfers aerodynamic forces to the structure. Understanding deformation and stress distribution in these components under realistic flight conditions is essential for structural integrity, weight reduction, and assessing aeroelastic instabilities.

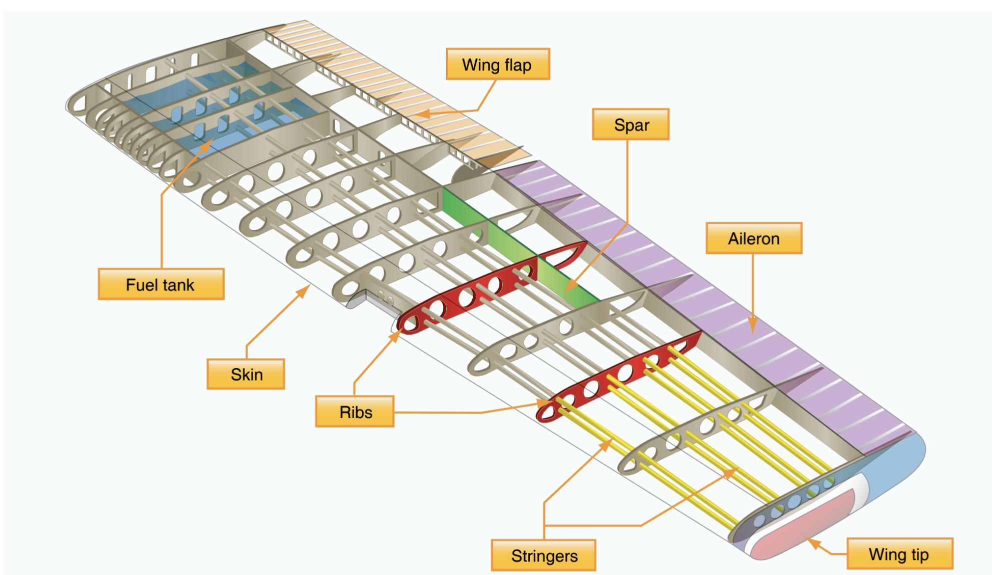

Figure 1: Primary components of an aircraft wing structure [1].

A common starting point for analysis is a *one-way fluid-structure interaction (FSI)* approach. In this method, the pressure distribution from a computational fluid dynamics (CFD) simulation on a rigid wing is applied as a static load to a finite element analysis (FEA) model of the structure. In one-way FSI, the structural deformation calculated by the FEA does not feed back to influence the aerodynamic solution. However, the reality of flight involves a fully coupled interplay between the flexible structure and the surrounding airflow. This phenomenon, known as *two-way FSI* or aero-structural coupling, involves a continuous feedback loop: the wing deforms under aerodynamic loads, the deformed shape alters the airflow and pressure distribution, the updated loads cause further deformation, and this process iterates until a converged state of equilibrium is reached [2, 3].

Figure 2 illustrates how structural sizing (an optimization process) integrates with these two FSI methodologies. In the one-way sizing approach (Fig. 2a), a fixed aerodynamic load from CFD is used. A structural optimization loop is then performed, where FEA is run repeatedly while structural parameters (e.g., panel thicknesses) are adjusted in a sizing process until an optimized structure is achieved for that specific, unchanging load case. Conversely, the two-way sizing approach (Fig. 2b) embeds the coupled CFD-FEA analysis within the optimization loop. For each design proposed by the sizing algorithm, a full two-way FSI analysis is conducted to find the converged aero-structural state, ensuring that the structure is optimized for the loads it experiences in its deformed, in-flight condition and yielding a more accurate, robust design.

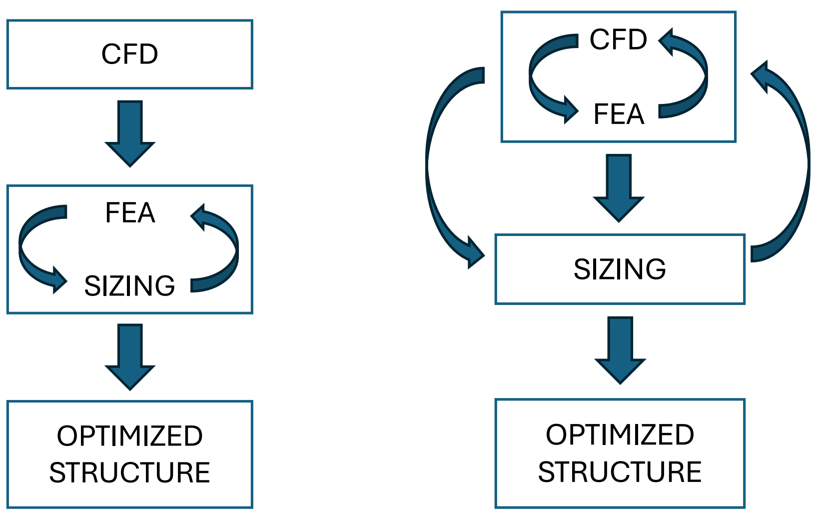

(a) One-way FSI

(b) Two-way FSI.

Figure 2: Conceptual workflows for structural sizing via one-way and two-way FSI.

Structural sizing is the optimization process of determining the dimensions of structural components (e.g., skin thickness, spar cross-sections) to produce an optimal design. The primary goal is typically to minimize structural mass while satisfying constraints, such as allowable stress, deformation, and buckling limits. This process can be done through manual iterations guided by engineering judgment or via automated process driven by numerical optimization algorithms.

In this project, structural sizing is performed only within a one-way FSI framework, using an adaptive single-objective optimization procedure (Kriging + MISQP). Two-way FSI is not used for sizing; instead, the optimized structure from the one-way FSI sizing will be assessed with a coupled two-way FSI analysis to compare the resulting drag, lift, maximum von Mises stress, and wing tip deflection. All the workflow from geometry preparation, CFD and FEA analyses, optimization algorithm, as well as the system coupling are performed within ANSYS Workbench [6].

1.2 Problem Description

The subject of this study is the wing structure of the Piper PA-38 Tomahawk [4], a two-seat, fixed-tricycle-gear general aviation airplane, shown in Fig. 3. The PA-38 features a rectangular planform with a constant chord, utilizing the NASA GA(W)-1 (or LS(1)-417) low-speed airfoil. The relevant aircraft specifications and wing geometric parameters are summarized in Table 1.

Table 1: Piper PA-38 Tomahawk Wing Specifications and Geometry.

Parameter	**Value**
Aircraft Name	Piper PA-38 Tomahawk
Maximum Take-Off Weight (MTOW)	757 kg
Cruise Speed	185 km/h (51.39 m/s)
Cruise Altitude	10 500 ft (3200 m)
Wing Half Planform	
Airfoil	NASA GA(W)-1 / LS(1)-417
Half Span ($b/2$)	5.18 m
Chord Length (c)	1.12 m
Planform Area (Half)	$5.80\,\mathrm{m}^2$

The structural model is a cantilevered half-wing with a closed wingbox formed by upper and lower skins, two spanwise spars, and ten chordwise ribs. All components are made from the isotropic aerospace-grade Aluminum 2024-T3 [5] with Young's modulus $E = 72.39\,\mathrm{GPa}$, Poisson's ratio $\nu = 0.33$, and density $\rho = 2768\,\mathrm{kg/m^3}$. As shown in Fig. 3b, the wingbox is bounded chordwise by two spars at 25% ($x = 0.280\,\mathrm{m}$) and 65% ($x = 0.728\,\mathrm{m}$) of the chord, and spanwise by ten ribs: a root rib at $z = 0$, a tip rib at $z = 5.18\,\mathrm{m}$, and eight intermediate ribs whose spanwise locations are design variables. These ribs define nine spanwise bays. Within the wingbox, the upper and lower skins between the spars are divided into nine panels, each corresponding to one bay, and the skins in each bay are assumed to have the same thickness. The optimization treats as design variables the thicknesses of the ten ribs, the two spars, and the nine skin panels (one thickness per bay, applied to both upper and lower skins between the spars as well as the blunt trailing edge face).

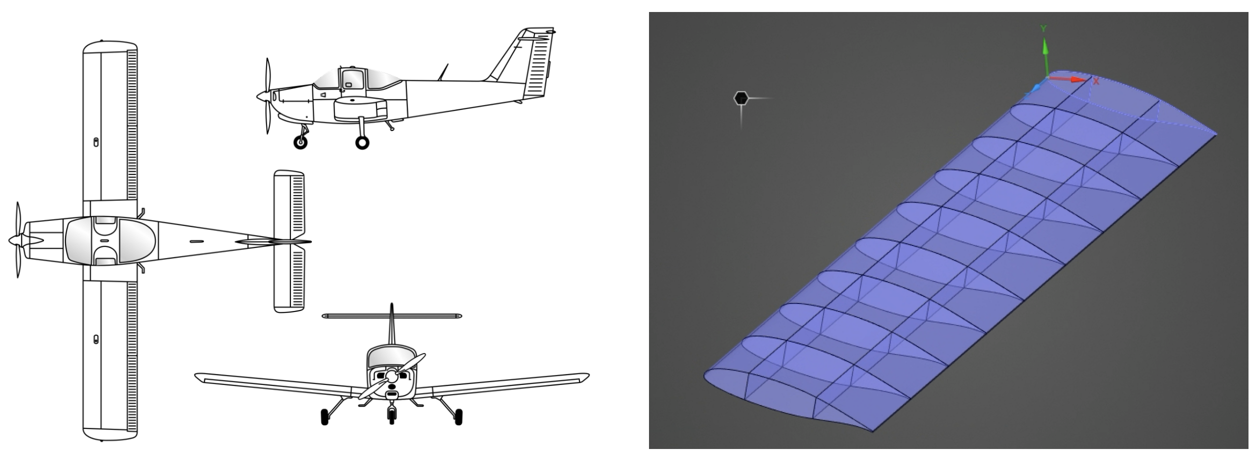

(a) Piper PA-38 three-view drawing. (b) Wing structure model (ribs, spars, and skin).

Figure 3: Geometry and structural configuration of the Piper PA-38 Tomahawk.

2 Methodology

2.1 Governing Equations

2.1.1 Linear Elasticity

The governing equations for the static structural analysis in this project is based on the well-known linear elasticity theory [7]. First, let $\boldsymbol{u} : \Omega_s \to \mathbb{R}^3$ be the displacement in the solid domain Ω_s with boundary $\partial\Omega_s = \Gamma_{\text{root}} \cup \Gamma_{\text{skin}}$. The small-strain tensor ($\boldsymbol{\varepsilon}$) is written from the kinematic relation:

$$\boldsymbol{\varepsilon}(\boldsymbol{u}) = \frac{1}{2}\left(\nabla\boldsymbol{u} + \nabla\boldsymbol{u}^{\mathsf{T}}\right), \tag{1}$$

where $\boldsymbol{u}$ is the displacement vector.

Second, the constitutive law, which describes the intrinsic behavior of the material is written in general form as

$$\boldsymbol{\sigma} = \mathbb{C} : \boldsymbol{\varepsilon}, \tag{2}$$

where $\boldsymbol{\sigma}$ is the Cauchy stress tensor, $\mathbb{C}$ is the fourth-order elasticity tensor in its general form with 81 constants. For isotropic material (its properties are the same in all directions), the above reduces to the following equation:

$$\boldsymbol{\sigma} = 2G\,\boldsymbol{\varepsilon} + \lambda\,\mathrm{tr}(\boldsymbol{\varepsilon})\,\mathbf{I}, \tag{3}$$

where G is the shear modulus, λ is the Lamé's first parameter, $\mathrm{tr}(\boldsymbol{\varepsilon})$ is the trace of the strain tensor, and $\mathbf{I}$ is the second-order identity tensor. In essence, this equation is the generalized 3D version of Hooke's law ($F = k\,x$). The parameters G and λ can be calculated as

$$G = \frac{E}{2(1+\nu)}, \qquad \lambda = \frac{E\nu}{(1+\nu)(1-2\nu)}, \tag{4}$$

where E is the Young's modulus and ν is the Poisson's ratio.

Lastly, since it is a static analysis, the following equation ensures that the body is in static equilibrium:

$$\nabla \cdot \boldsymbol{\sigma} + \boldsymbol{b} = \mathbf{0} \quad \text{in } \Omega_s, \tag{5}$$

where $\nabla \cdot \boldsymbol{\sigma}$ is the divergence of the stress tensor, which represents the net internal force per unit volume, and $\boldsymbol{b}$ is the body force vector, such as the body weight due to gravity $\boldsymbol{b} = \rho\boldsymbol{g}$.

Combining all the equations above, the following equation can be derived for isotropic case, which is known as the Navier-Cauchy equation:

$$(G+\lambda)\nabla(\nabla\cdot\boldsymbol{u}) + G\nabla^2\boldsymbol{u} + \boldsymbol{b} = \mathbf{0}, \tag{6}$$

where $\nabla^2\boldsymbol{u}$ is the vector Laplacian. This is the *core governing equation*, which is a second-order partial differential equation (PDE) for the displacement vector field $\boldsymbol{u}$. It is this equation that Finite Element Method (FEM) software such as ANSYS [6] is designed to solve numerically. The software takes this PDE, the geometry of the domain Ω, the material properties (E, ν), and the boundary conditions (e.g., fixed supports and applied pressures) as input, and computes the displacement field $\boldsymbol{u}$ throughout the entire wing structure. Once $\boldsymbol{u}$ is known, the strain $\boldsymbol{\varepsilon}$ can be calculated using the kinematic relation, and subsequently, the stress $\boldsymbol{\sigma}$ can be found using the constitutive law, completing the analysis.

2.1.2 Aerodynamics

For the fluid analysis, the compressible Navier-Stokes (NS) equations are solved to determine the flow field around the wing. The conservation form of the equations is written as:

$$\frac{\partial \mathbf{U}}{\partial t} + \nabla \cdot \mathbf{F}_c(\mathbf{U}) - \nabla \cdot \mathbf{F}_v(\mathbf{U}, \nabla \mathbf{U}) = \mathbf{Q}(\mathbf{U}) \quad \text{in } \Omega_f, \tag{7}$$

where Ω_f is the fluid domain, $\mathbf{U}$ represents the vector of conservative state variables (mass, momentum, and energy), $\mathbf{F}_c(\mathbf{U})$ is the convective flux, $\mathbf{F}_v(\mathbf{U}, \nabla\mathbf{U})$ is the viscous flux, and $\mathbf{Q}(\mathbf{U})$ is a generic source term. To make the simulation computationally feasible, the Reynolds-Averaged Navier-Stokes (RANS) approach is employed [8]. This method decomposes the instantaneous flow variables into a time-averaged component and a fluctuating component, resulting in additional terms known as Reynolds stresses that require modeling to close the system of equations. In this project, the turbulence closure is provided by the Shear Stress Transport (SST) $k-\omega$ model [9]. Details are omitted since they are outside the scope of the course.

2.2 Loads and Boundary Conditions

The structural analysis models the wing as a cantilever beam, fully constrained at the root surface (Γ_{root}). The loading environment combines inertial effects with aerodynamic forces. To account for the self-weight of the wing structure during maneuvers, a vertical acceleration field $\boldsymbol{a}$ is applied to the entire domain Ω. The magnitude of this acceleration is defined as $n \cdot g$, where n is the load factor and $g = 9.81\,\text{m/s}^2$. For the critical 3G pull-up maneuver ($n = 3$), this results in a vertical acceleration of $29.43\,\text{m/s}^2$. Simultaneously, the aerodynamic pressure distribution corresponding to the specific flight condition is applied to the external skin (Γ_{skin}). The governing boundary value problem is summarized as follows:

$$\boldsymbol{u} = \mathbf{0} \qquad \text{on } \Gamma_{\text{root}}, \tag{8}$$

$$\boldsymbol{\sigma}\,\boldsymbol{n} = -p(\boldsymbol{x})\,\boldsymbol{n} \qquad \text{on } \Gamma_{\text{skin}}, \tag{9}$$

$$\boldsymbol{f}_{\text{body}} = \rho_s \boldsymbol{a} \qquad \text{in } \Omega_s. \tag{10}$$

Figure 4a shows the root fixed support, inertial load direction, and imported pressure region. Aerodynamic pressures, derived from CFD, are mapped onto the non-conformal structural mesh using an interpolation algorithm. Figure 4b illustrates this projection of the pressure point cloud onto the finite element nodes

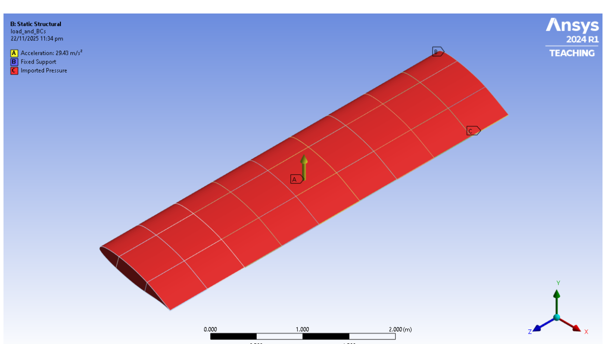

(a) Loads and BCs.

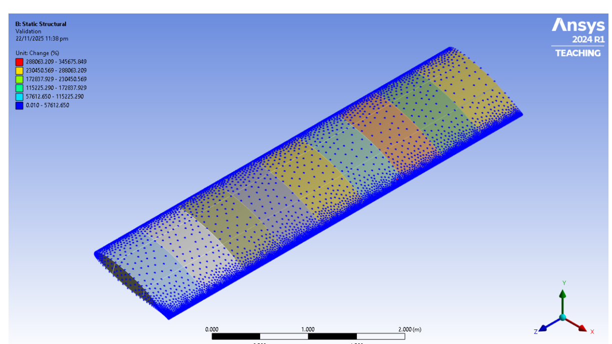

(b) Interpolation of aerodynamic pressure data.

Figure 4: Overview of the structural boundary conditions and the pressure mapping strategy.

2.3 Aerodynamic Analysis and Load Case Selection

To determine the aerodynamic loads, CFD analyses were performed in ANSYS Fluent. The fluid domain is discretized using an unstructured tetrahedral mesh, as shown in Fig.5. Figure 5b illustrates the far-field boundaries, while Fig. 5a details the refinement near the wing surface. The total mesh count is approximately 760,000 cells. While this resolution (particularly in the wake region trailing the airfoil) may not be sufficient for high-fidelity drag prediction, it is considered adequate for capturing the surface pressure distribution required for structural sizing.

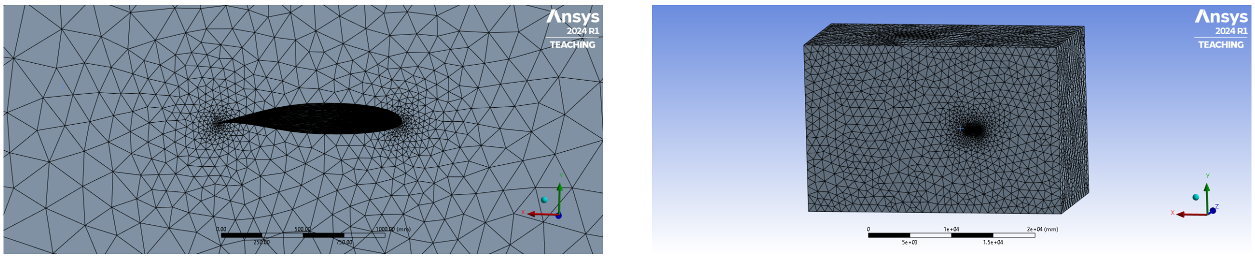

(a) Near-field mesh refinement. (b) Far-field domain.

Figure 5: Unstructured mesh used for the CFD analysis, comprising approximately 760,000 cells.

The simulations were conducted at the aircraft's cruise altitude of 10 500 ft (3200 m). At this altitude, the standard atmospheric properties are a density of $\rho = 0.89\,\mathrm{kg/m^3}$ and a dynamic viscosity of $\mu = 1.69 \times 10^{-5}\,\mathrm{kg/(m \cdot s)}$. The freestream velocity was set to the cruise speed of 51.39 m/s. An angle of attack (AoA) sweep was performed from 0° to 16° (pre-stall condition) to generate the aerodynamic polar curves. Figures 6a and 6b present the lift coefficient (C_L) and drag coefficient (C_D) versus AoA, respectively. These polars are essential for identifying the specific angles of attack corresponding to the required structural load factors.

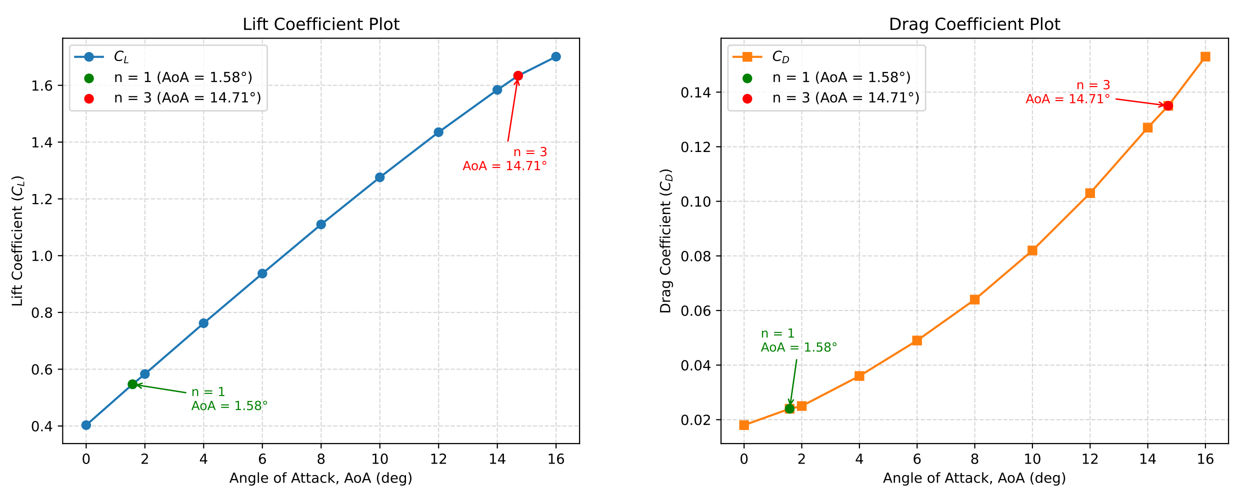

(a) Lift Coefficient (C_L) vs. AoA. (b) Drag Coefficient (C_D) vs. AoA.

Figure 6: Aerodynamic polar curves obtained from the CFD analysis.

The structural design load is determined by the load factor n, defined as the ratio of the lift force L to the aircraft weight W:

$$n = \frac{L}{W} = \frac{L}{m_{\mathrm{MTOW}}\, g}. \tag{11}$$

Assuming the wing generates the entirety of the lift required to sustain the aircraft, the target lift for the half-wing model is calculated as:

$$L_{\text{half}} = n \cdot \frac{m_{\text{MTOW}} \cdot g}{2}. \tag{12}$$

Two specific flight conditions were isolated from the polar data:

1. **Steady Level Flight ($n = 1$):** This corresponds to the standard cruise condition. Based on the interpolation of the C_L curve, this state is achieved at an AoA of 1.58°.

2. **Pull-up Maneuver ($n = 3$):** This represents a high-g maneuver where the structure must support three times the aircraft's static weight. This condition is met at an AoA of 14.71°.

The pressure distributions at the wing root for these two conditions are visualized in Fig. 7. Figure 7a shows the pressure field for the 1G cruise condition, while Fig. 7b displays the significantly higher suction peaks and pressure differentials associated with the 3G maneuver.

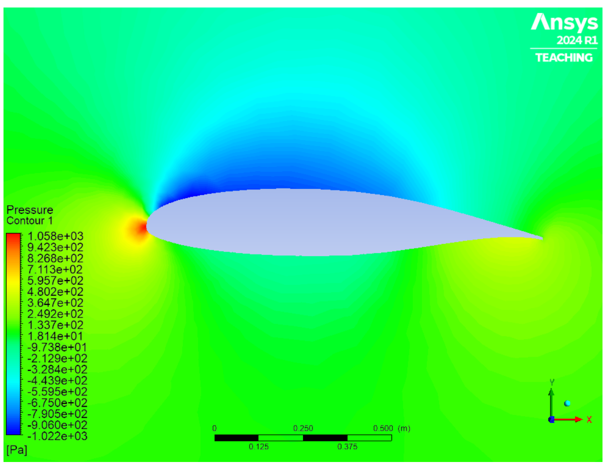

(a) Pressure contour at 1G (AoA = 1.58°).

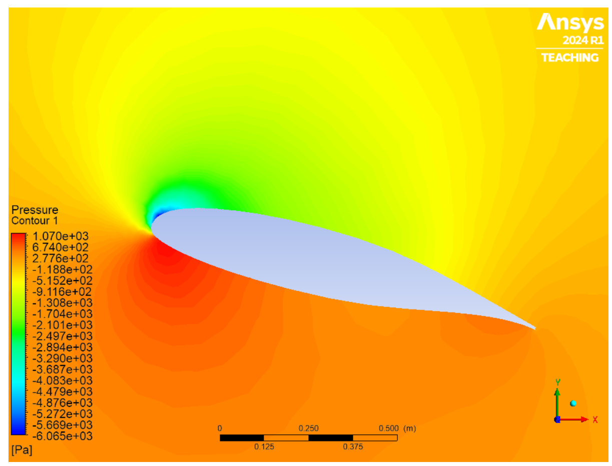

(b) Pressure contour at 3G (AoA = 14.71°).

Figure 7: Comparison of pressure distributions at the wing root for cruise and maneuver conditions.

For the structural sizing optimization, the $n = 3$ (3G) load case was selected as the design condition. This assumption is made because the 3G maneuver represents the upper limit of the loads the structure is expected to withstand during operation; a wing sized to survive this condition will inherently satisfy the requirements for steady level flight. Consequently, the 3D pressure field from the $n = 3$ CFD solution was mapped onto the external skin of the structural finite element model. Figure 8 depicts this mapped pressure distribution on the upper surface of the wing, which serves as the primary boundary condition for the subsequent stress analyses.

2.4 Finite Element Mesh

The structural domain is discretized using the Finite Element Method (FEM) within ANSYS Mechanical. Given the thin-walled nature of the aircraft wing components (comprising the skins, spars, and ribs), shell elements are employed to model the geometry efficiently. Specifically, the `SHELL181` element type is selected. This is a 4-node linear shell element with six degrees of freedom at each node, suitable for analyzing thin to moderately thick shell structures.

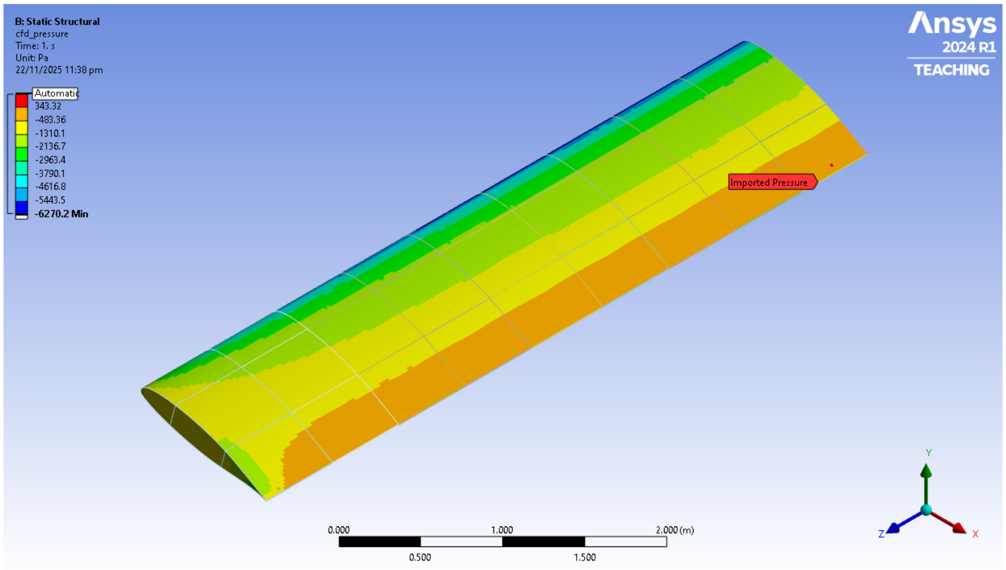

Figure 8: Aerodynamic pressure distribution for the 3G load case mapped onto the FEA model.

A global mesh sizing of 20 mm is applied to all components. This element size was selected based on a Grid Convergence Study, the details of which are presented in a subsequent section, ensuring that the discretization error is minimized while maintaining computational efficiency.

A critical aspect of the model setup is the topology handling. The geometry is constructed with shared topology, meaning that the geometric faces of intersecting components (e.g., the junction between a rib and a spar, or the skin and the internal structure) share common edges. Consequently, the meshing algorithm generates coincident nodes at these interfaces. This approach ensures perfect displacement continuity and load transfer between components without the need for defining contact elements (such as bonded contacts), thereby reducing model complexity and solution time.

The resulting finite element mesh is visualized in Fig. 9. Figure 9a depicts the discretization of the external skin, highlighting the curvature capture of the airfoil, while Fig. 9b illustrates the mesh quality of the internal ribs and spars.

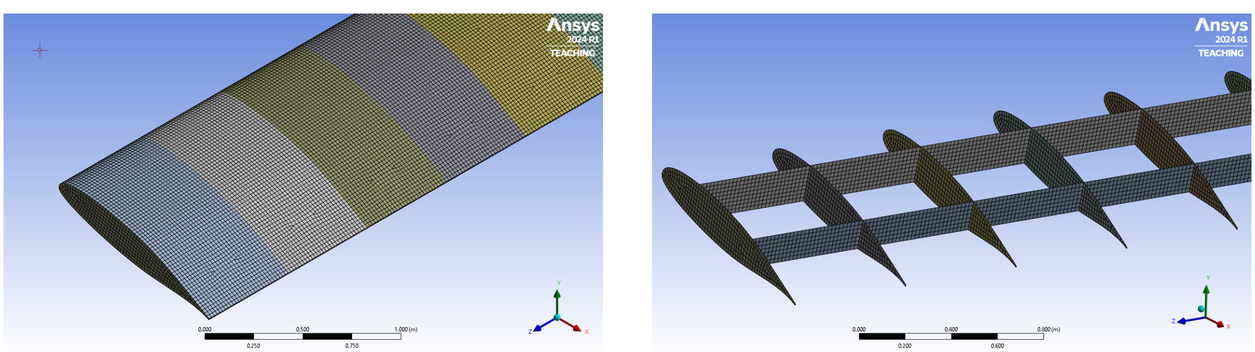

(a) External skin mesh.

(b) Internal structure mesh (ribs and spars).

Figure 9: Finite element mesh using `SHELL181` elements with a global size of 20 mm.

2.5 Metrics of Interest

Four key metrics are evaluated to assess the performance and safety of the wing design. The first is the wing structural mass (M_{wing}), which serves as the primary minimization objective. This is calculated within ANSYS by summing the product of element area, thickness, and the uniform material density. The second metric is the maximum von Mises stress ($\sigma_{\text{vM,max}}$). Under the plane stress assumption for shell elements ($\sigma_z = \tau_{yz} = \tau_{zx} = 0$), the equivalent stress is calculated as:

$$\sigma_{\text{vM}} = \sqrt{\sigma_x^2 + \sigma_y^2 - \sigma_x \sigma_y + 3\tau_{xy}^2}. \tag{13}$$

The third metric is the wing tip deflection (w_{tip}), defined as the maximum directional deformation in the vertical (Y) axis, which indicates the structure's stiffness. Finally, a Factor of Safety (FoS) is derived to quantify the margin against failure. Using the yield strength of Al 2024-T3 ($S_y = 324\,\text{MPa}$), the FoS is defined as:

$$\text{FoS} = \frac{S_y}{\sigma_{\text{vM,max}}}. \tag{14}$$

An FoS > 1 is required to ensure the material remains within the elastic region.

2.6 Design and Analysis Phases

The structural design and assessment process is organized into three distinct phases, preceded by a preliminary verification step. Initially, a **Grid Convergence Study** is conducted to establish a global mesh size that ensures solution accuracy while maintaining computational efficiency. Following this, the project proceeds through three sequential phases:

1. **Rib Layout Selection:** The first problem determines the optimal configuration of the internal structure. While the root and tip ribs are fixed, the spanwise locations of the eight intermediate ribs are varied. A set of manually proposed layout candidates is evaluated, and the one yielding the highest Factor of Safety (FoS) is selected as the baseline geometry.

2. **Structural Sizing Optimization:** Using the optimal rib layout from the first problem, this phase employs an automated numerical optimization algorithm to determine the optimal thickness distribution for the skin panels, spars, and ribs. The objective is to minimize structural mass while satisfying safety constraints. This process is performed using the one-way FSI approach (see Fig. 2a).

3. **Aerostructural Coupling Assessment (Two-Way FSI):** The final problem investigates the validity of the sizing results under coupled conditions. The mass-optimized structure obtained from the second problem is subjected to a fully coupled two-way FSI analysis. The resulting aerodynamic loads and structural responses are compared against the one-way FSI predictions to quantify the effects of static aero-structural coupling.

3 Grid Convergence Study

To ensure sufficient solution accuracy while maintaining computational efficiency, a mesh refinement study was performed on the structural finite element model. The global shell element size was varied from 100 mm to 10 mm, and the corresponding number of elements, wing tip deflection, and maximum von Mises stress were recorded. The results are summarized in Table 2 and Fig. 10.

Table 2: Grid Convergence Study Results.

Mesh	**Level**	**Size** (mm)	**Elements**	**Nodes**	**Tip Deflection** (mm)	**Max Stress** (MPa)
L9	1	100	1766	1545	175.45	197.70
L8	2	50	6603	6137	169.00	202.78
L7	3	40	9770	9192	167.66	210.16
L6	4	35	12 564	11 906	167.28	215.07
L5	5	30	17 359	16 583	167.23	221.81
L4	6	25	24 827	23 890	167.35	227.78
L3	7	20	39 388	38 187	167.37	243.27
L2	8	15	68 502	66 895	167.47	253.18
L1	9	10	153 294	150 840	166.99	270.85

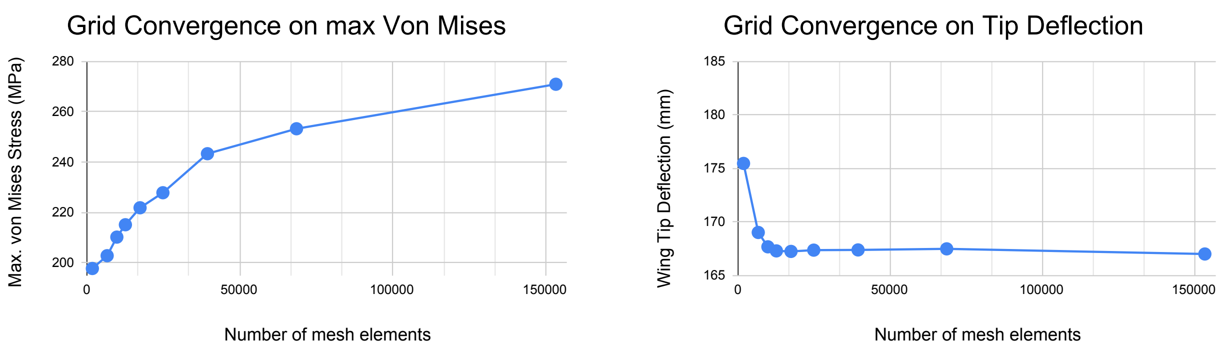

(a) Max. von Mises Stress

(b) Wing Tip Deflection

Figure 10: Grid convergence metrics (Deflection and Stress) vs. Number of Mesh Elements.

As shown in the table, a strong mesh dependency is visible at coarse mesh levels (L9–L7), where the predicted tip deflection reduces significantly from 175.45 mm (100 mm mesh) to 167.66 mm (40 mm mesh). Beyond a global element size of 35 mm, both response quantities begin to plateau. The tip deflection remains within a narrow range of 167.23 mm to 167.47 mm for mesh sizes between 30 mm to 15 mm, showing variations below 0.15%. Similarly, the maximum von Mises stress exhibits monotonic hardening with mesh refinement—typical of shell-element models—as stress hotspots become better resolved. The stress increases from 197.7 MPa at the coarsest mesh to 243.27 MPa at the 20 mm mesh level. Subsequent refinement to 15 mm and 10 mm continues increasing the stress, though with diminishing improvement relative to computational cost.

A 20 mm global element size (Mesh Level L3) was selected as it provides converged deflection, acceptable stress accuracy, and over 60% reduced computational cost compared to finer meshes.

4 Phase 1: Rib Layout Selection

4.1 Problem Setup

The goal of Phase 1 is to determine the optimal arrangement of the eight intermediate ribs along the wingspan. While the root and tip ribs are fixed, the remaining ribs may be redistributed to improve structural performance under the 3G design load case.

As shown in Fig. 11, six rib-layout strategies were evaluated, including: Baseline uniform spacing, Root-clustered strong, Root-clustered mild, Root-clustered geometric, Two-zone configuration, and Tip-clustered. Each layout preserves ten total ribs but alters the spanwise locations of Ribs 1–8 using clustering parameters. All geometric models were meshed using the previously validated 20 mm shell element size, ensuring consistency across the study.

For each configuration, the following structural response metrics were extracted: total structural mass (kg), maximum von Mises stress (MPa), wing tip vertical deflection (mm), and Factor of Safety (FoS). The Factor of Safety is based on the material yield stress of Aluminum 2024-T3 (324 MPa), using:

$$\text{FoS} = \frac{324}{\sigma_{\text{vM,max}}}. \tag{15}$$

The goal of Phase 1 is to select the rib layout with the best structural performance—primarily high FoS and low deflection—while maintaining equal rib thicknesses (1.0 mm) across all configurations.

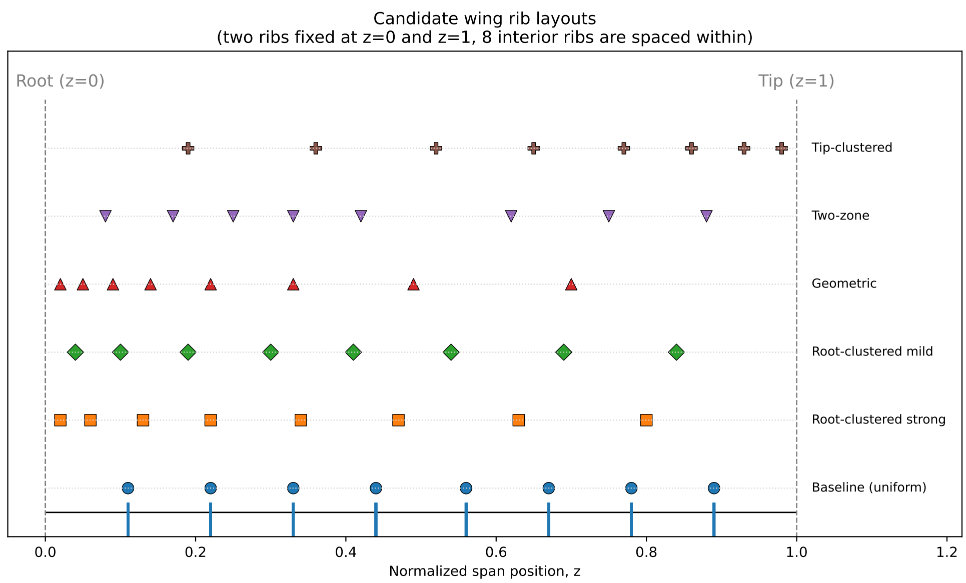

Figure 11: Visualization of the six rib-layout strategies evaluated.

4.2 Results and Discussion

Table 3 summarizes the structural performance of all six rib layouts. Several key trends emerge regarding stiffness and strength.

Across all six rib configurations, the wing tip deflection remains within a narrow range of 166.91 mm to 167.38 mm. This indicates that rib spacing has minimal influence on global bending stiffness, which is dominated primarily by the spars and skins rather than the rib positions.

Figure 12 visually compares the deformation of the internal structures. The Baseline layout (Fig. 12a) exhibits a tip deflection of 167.37 mm, while the Root-clustered strong layout (Fig. 12b) shows a marginally lower deflection of 166.99 mm. The visual comparison of the ribs highlights the higher density of structural members near the root in the clustered configuration, though the global curvature remains nearly identical.

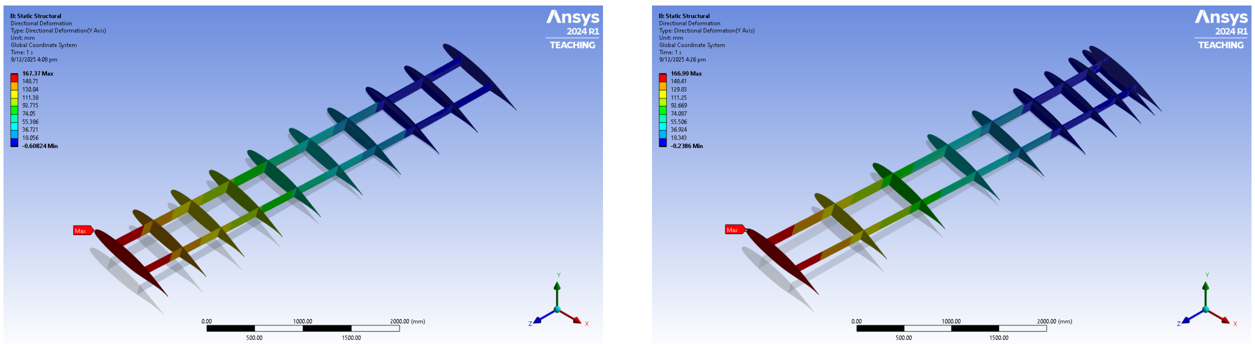

(a) Baseline (Uniform): 167.37 mm

(b) Root-clustered Strong: 166.99 mm

Figure 12: Comparison of wing tip deflection and internal rib arrangement (skin hidden for clarity).

In contrast to deflection, the maximum von Mises stress shows clear sensitivity to rib layout. The baseline uniform arrangement produces the highest stress (243.27 MPa), whereas Root-clustered configurations reduce stress by improving load redistribution near the wing root.

This improvement is illustrated in Fig. 13. The Baseline layout (Fig. 13a) exhibits a large region of high stress (red/orange contours) on the upper skin near the root. By shifting ribs toward this critical area, the Root-clustered strong layout (Fig. 13b) effectively relieves the skin panels, reducing the peak stress to 221.08 MPa.

Consequently, the Factor of Safety follows this same trend: the baseline layout provides the minimum FoS (1.33), while the root-clustered strong layout achieves the highest value (1.47). Since all designs use identical component thicknesses, mass remains fixed at 42 kg. Overall, the **Root-clustered strong** layout offers the most favorable structural performance and is therefore selected as the geometric baseline for the subsequent sizing optimization phase.

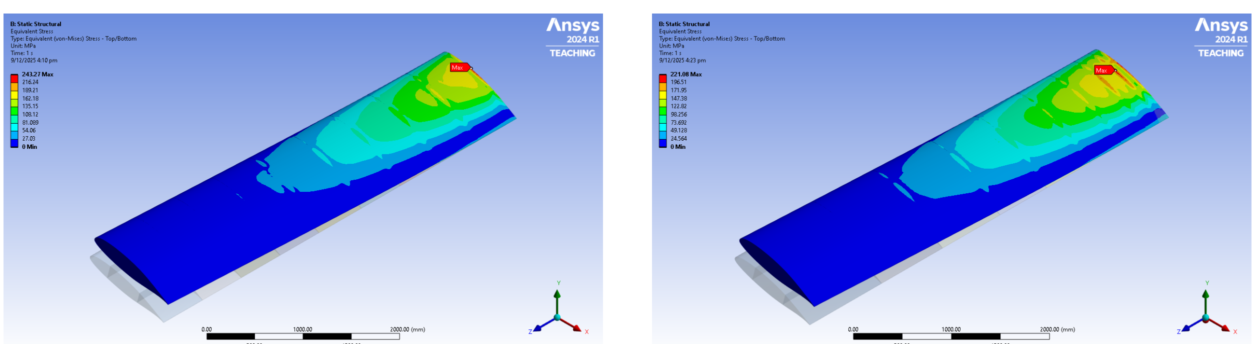

(a) Baseline (Uniform): 243.27 MPa

(b) Root-clustered Strong: 221.08 MPa

Figure 13: Comparison of maximum von Mises stress distributions.

Table 3: Performance comparison of different rib layout strategies.

Layout Name	Intermediate Rib Locations (Normalized Span)								Mass	Stress	Deflection	FoS
	R1	R2	R3	R4	R5	R6	R7	R8	(kg)	(MPa)	(mm)	
Baseline (uniform)	0.11	0.22	0.33	0.44	0.56	0.67	0.78	0.89	42	243.27	167.37	1.33
Root-clustered strong	0.02	0.06	0.13	0.22	0.34	0.47	0.63	0.80	42	221.08	167.00	1.47
Root-clustered mild	0.04	0.10	0.19	0.30	0.41	0.54	0.69	0.84	42	238.57	167.21	1.36
Root-clustered geometric	0.02	0.05	0.09	0.14	0.22	0.33	0.49	0.70	42	221.66	167.05	1.46
Two-zone	0.08	0.17	0.25	0.33	0.42	0.63	0.75	0.88	42	241.54	167.38	1.34
Tip-clustered	0.19	0.36	0.52	0.65	0.77	0.86	0.93	0.98	42	246.23	166.91	1.32

5 Phase 2: Structural Sizing Optimization

5.1 Problem Setup

Based on Phase 1 results, the "Root-clustered strong" internal layout is selected for structural sizing. A baseline design is established with a uniform thickness of 1.0 mm for all ribs, spars, and skin panels. Under the critical 3G load case, this baseline is infeasible: although the structural mass is 42.0 kg, the minimum Factor of Safety (FoS) is 1.46 (violating FoS ≥ 1.5) and the maximum vertical tip deflection is 166.99 mm. The deflection limit of 150 mm corresponds to approximately 3% of the wing semi-span, a constraint imposed to ensure linear structural behavior and prevent excessive aeroelastic deformation. Consequently, numerical optimization is required to redistribute material thickness to minimize mass while satisfying these safety and stiffness criteria.

The optimization problem involves 21 design variables representing component thicknesses. Let $\mathbf{x} \in \mathbb{R}^{21}$ be the design vector:

$$\mathbf{x} = [t_{\text{rib},1}, \ldots, t_{\text{rib},10},\ t_{\text{spar},1}, t_{\text{spar},2},\ t_{\text{skin},1}, \ldots, t_{\text{skin},9}]^{\mathsf{T}}. \tag{16}$$

The mathematical formulation is defined as:

$$\begin{aligned}
\min_{\mathbf{x}\in\mathbb{R}^{21}} \quad & M_{\text{wing}}(\mathbf{x}) && (17)\\
\text{subject to} \quad & \text{FoS}(\mathbf{x}) = \frac{\sigma_y}{\sigma_{\max}(\mathbf{x})} \geq 1.5 \iff \sigma_{\max}(\mathbf{x}) \leq \frac{\sigma_y}{1.5}, && (18)\\
& \delta_{\text{tip}}(\mathbf{x}) \leq 150\,\text{mm} \quad \text{(vertical component)}, && (19)\\
& 0.5\,\text{mm} \leq t_{\text{rib},i} \leq 3.0\,\text{mm}, \quad i = 1(\text{root}), \ldots, 10(\text{tip}), && (20)\\
& 0.5\,\text{mm} \leq t_{\text{spar},j} \leq 5.0\,\text{mm}, \quad j = 1(\text{front}), 2(\text{rear}), && (21)\\
& 0.5\,\text{mm} \leq t_{\text{skin},k} \leq 5.0\,\text{mm}, \quad k = 1(\text{root}), \ldots, 9(\text{tip}). && (22)
\end{aligned}$$

Here, $M_{\text{wing}}(\mathbf{x})$ is the wing structural mass, $\sigma_{\max}$ is the maximum von Mises stress, and δ_{tip} is the vertical tip deflection. Material properties for Al 2024-T3 are $\rho = 2768\,\text{kg/m}^3$ and $\sigma_y = 324\,\text{MPa}$.

The optimization is performed using the Adaptive Single-Objective method in ANSYS. This approach utilizes a Kriging surrogate model [10] to approximate the design space, coupled with a Mixed-Integer Sequential Quadratic Programming (MISQP) optimizer. The surrogate is constructed using an Optimal Space Filling (OSF) design of experiments, initialized with 150 samples and augmented with 350 infill samples, allowing for a maximum of 500 design iterations to locate the global optimum.

5.2 Results and Discussion

5.2.1 Optimization History

The optimization history utilizing the Adaptive Single-Objective method is visualized in Fig. 14. The scatter plot tracks the wing structural mass across 500 iterations. Points marked in red represent infeasible designs (violating either FoS or deflection constraints), while green points represent feasible designs. The blue line tracks the convergence of the best feasible design found so far.

The process begins with an OSF design of experiment (first 150 samples). During this phase, the mass fluctuates significantly and remains relatively high as the algorithm explores the boundaries of the design space rather than minimizing the objective immediately. Following the exploration phase, the MISQP optimizer takes over, and the wing structural mass begins to decrease steadily. The baseline design (DP 0), indicated by a red star, is shown to be infeasible with a mass of 42.0 kg. The global optimum was identified at Design Point (DP) 482.

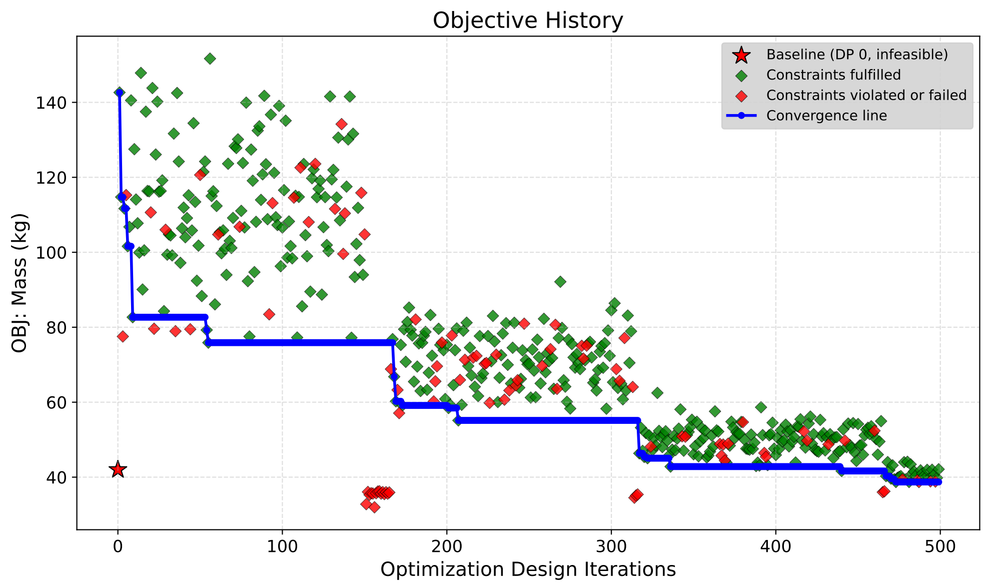

Figure 14: Optimization history showing feasible (green) and infeasible (red) design points, with the convergence trajectory (blue).

5.2.2 Comparison Between Baseline (DP 0) and Best Feasible Design (DP 482)

A direct comparison between the Baseline (DP 0) and the Best Feasible Design (DP 482) is presented in Table 4 and Fig. 15. The baseline design utilized a uniform thickness of 1.0 mm, resulting in a violation of both the Factor of Safety (FoS) and stiffness constraints.

The optimized design (DP 482) successfully reduced the structural mass by approximately 7.8%, lowering it from 42.0 kg to 38.7 kg. Crucially, this mass reduction was achieved while simultaneously improving structural integrity. The FoS increased from 1.46 to 1.99, and the maximum vertical tip deflection decreased from 166.99 mm to 148.84 mm, thereby satisfying the 150 mm limit. The resulting FoS (1.99) is significantly higher than the constraint boundary (1.5). This indicates that the design is stiffness-driven rather than strength-driven. The optimizer added material to limit tip deflection to 150 mm, inadvertently strengthening the wing beyond minimum yield requirements.

Table 4: Comparison of Objective and Constraints: Baseline vs. Optimized Design

Metric	Baseline (DP 0)	Best Feasible (DP 482)	Change
Mass	42.00 kg	38.71 kg	-7.8%
Tip Deflection	166.99 mm	148.84 mm	-10.9%
Max von Mises Stress	221.08 MPa	163.01 MPa	-26.3%
Factor of Safety (FoS)	1.46	1.99	+36.3%

The specific optimized thickness values for all structural components are detailed in Table 5. Figure 15b further illustrates the changes in component thickness relative to the 1.0 mm baseline. The results reveal a material distribution strategy that generally aligns with beam theory principles. Specifically, thicknesses for skin panels and ribs near the wing root (e.g., $t_{\text{skin},1-3}$, $t_{\text{rib},1-3}$) were increased to withstand the highest bending moments and shear forces, while components further outboard generally saw a reduction in thickness to save mass as internal loads decreased.

Table 5: Optimized Component Thicknesses for DP 482.

Skin Panel	t (mm)	Rib	t (mm)	Spar	t (mm)
Skin 1 (Root)	1.49	Rib 1 (Root)	1.48	Spar 1 (Front)	0.52
Skin 2	2.15	Rib 2	1.59	Spar 2 (Rear)	1.02
Skin 3	1.69	Rib 3	1.48		
Skin 4	1.20	Rib 4	0.83		
Skin 5	1.06	Rib 5	0.89		
Skin 6	0.89	Rib 6	0.73		
Skin 7	0.56	Rib 7	1.28		
Skin 8	0.54	Rib 8	0.89		
Skin 9 (Tip)	0.79	Rib 9	0.66		
		Rib 10 (Tip)	1.28		

However, as observed in Table 5 and Fig. 15b, the resulting thickness distribution is notably non-intuitive and "jagged." Exceptions to the general outboard reduction are observed at Rib 7 and Rib 10, where thickness was increased significantly compared to their neighbors. This suggests that these specific components play a critical role in maintaining the global torsional or bending stiffness required to satisfy the strict 150 mm deflection limit.

The thickness fluctuates between adjacent ribs rather than tapering smoothly. This occurs because the numerical optimizer exploits the mathematical surrogate model to find a local minimum that satisfies constraints, without regard for engineering "best practices" or manufacturing logic. While mathematically valid, such a jagged distribution is difficult to manufacture. To achieve a more practical design in future iterations, additional linear constraints should be formulated. These could include continuity constraints (e.g., $|t_i - t_{i+1}| \leq \delta$) to limit thickness jumps between panels, or monotonic constraints (e.g., $t_{\text{root}} \geq t_{\text{mid}} \geq t_{\text{tip}}$) to ensure a smooth structural taper.

The visual results from the FEA confirm the numerical improvements. Figure 16 compares the equivalent (von Mises) stress distributions. In both designs, the high-stress regions are concentrated near the root, consistent with cantilever wing behavior. However, the optimized design shows a lower peak stress (163 MPa) compared to the baseline (221 MPa). The Y-axis deformation is shown in Fig. 17. As expected, deformation increases with distance from the root. The optimized design exhibits a stiffer response, keeping the maximum deflection within the feasible range.

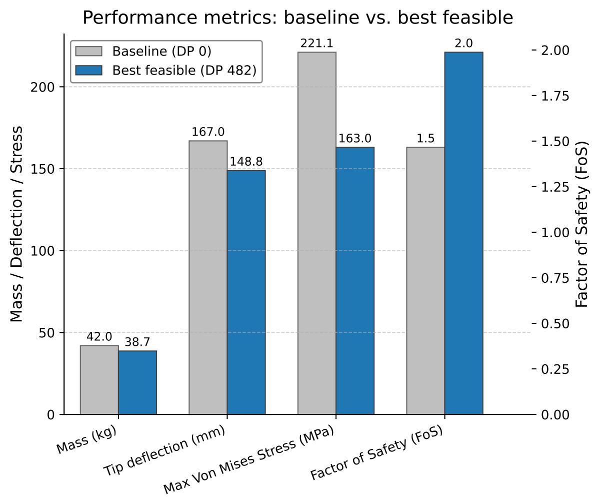

(a) Performance metrics comparison

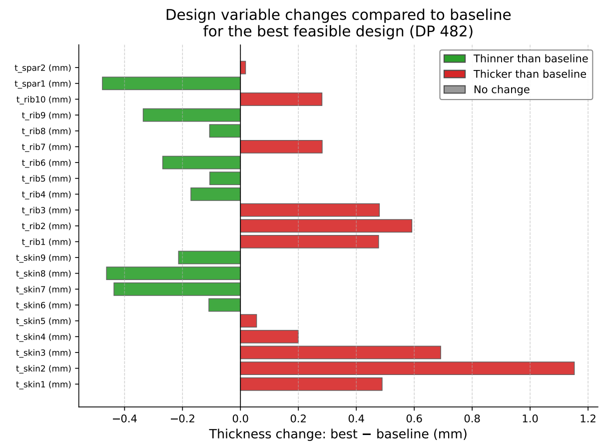

(b) Thickness deviations from baseline

Figure 15: Comparison between Baseline (DP 0) and Best Feasible Design (DP 482).

Finally, Fig. 18 highlights a distinct shift in the critical stress location between the two configurations. In the baseline design (Fig. 18a), the maximum stress is located on the upper skin surface near the second rib, suggesting that the uniform thin skin was buckling or yielding under compressive bending loads. In contrast, the optimized design (Fig. 18b) shows the maximum stress location shifted to the junction between the skin, root rib, and front spar, which is a region of high geometric stiffness due to the shared topology. This shift indicates that the optimizer successfully strengthened the skin panels, thereby forcing the critical load path into the robust root structure where the wing is constrained.

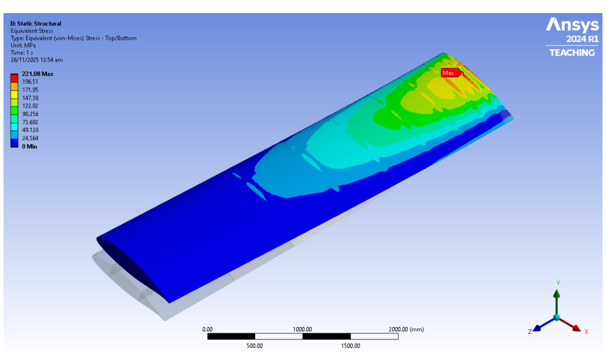

(a) Baseline (DP 0)

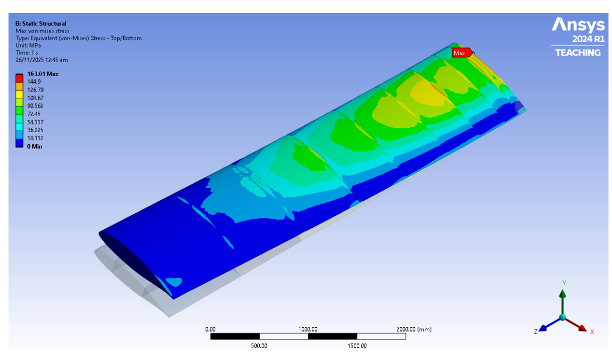

(b) Best Feasible (DP 482)

Figure 16: Equivalent von Mises stress distribution.

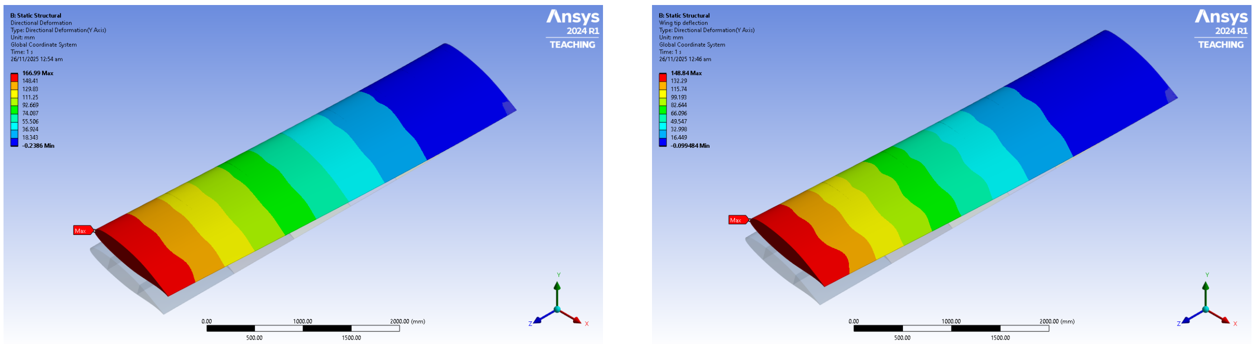

(a) Baseline (DP 0) (b) Best Feasible (DP 482)

Figure 17: Directional deformation (Y-axis) comparison.

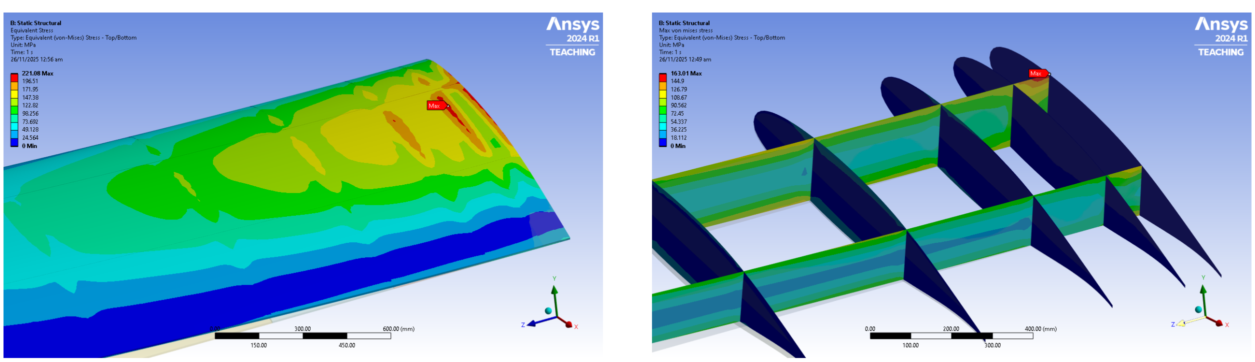

(a) Baseline (DP 0) (b) Best Feasible (DP 482)

Figure 18: Zoomed view of critical stress locations.

6 Phase 3: Aerostructural Coupling Assessment (Two-Way FSI)

6.1 Problem Setup

In Phase 3, the investigation focuses on the validity of the rigid-wing assumption employed during the structural sizing process. In the previous phases, the aerodynamic pressure distribution was derived from a CFD simulation of the rigid, undeformed wing geometry and mapped onto the structural model. This approach assumes that the structural deformation is negligible enough that it does not alter the surrounding flow field. However, in reality, the wing is a flexible structure; as it bends and twists under aerodynamic loads, the effective angle of attack and camber change. This deformation alters the pressure distribution, which in turn modifies the structural loads, creating a continuous feedback loop until a state of aeroelastic equilibrium is reached.

To quantify the impact of this phenomenon, the Best Feasible Design (DP 482) obtained from Phase 2 is subjected to a coupled two-way FSI analysis. It is important to note that, unlike the procedure in Phase 2, this phase does not involve an optimization loop. No design variables are modified, and no objective functions are minimized. Instead, the workflow consists of a single, high-fidelity coupled simulation intended solely to verify the structural response when aeroelastic effects are included, comparing these results against the one-way FSI predictions.

The integration of the solvers is managed within ANSYS Workbench. Figure 19 contrasts the project schematics for the two approaches. In the one-way framework (Fig. 19a), the solution flows unidirectionally from the CFD solver (Fluent) to the FEA solver (Static Structural). Conversely, the two-way FSI framework (Fig. 19b) utilizes the *System Coupling* component. As shown in the schematic, the coupling component manages the bi-directional data exchange between the solvers for this single analysis point, without the inclusion of a parameter optimization set.

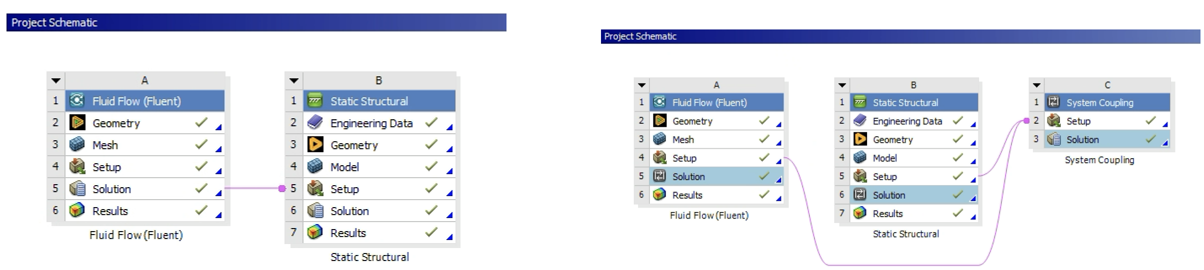

(a) One-way FSI workflow.

(b) Two-way FSI via System Coupling.

Figure 19: Comparison of ANSYS Workbench project FSI schematics: one-way vs two-way.

The boundary conditions are updated to support mesh motion and data transfer. In the fluid domain (ANSYS Fluent), the wing boundary is designated as a *System Coupling* region. To accommodate the deformation of the wing surface without degrading mesh quality, a *Dynamic Mesh* model is activated, employing smoothing methods to adjust the internal fluid nodes in response to boundary displacement. Simultaneously, in the structural domain (ANSYS Mechanical), a *System Coupling* region is also applied to the wing skin, designating it as the recipient of pressure loads and the source of deformation data. The coupling logic, defined within the System Coupling settings, manages the bidirectional data exchange where aerodynamic forces are transferred from the fluid to the structural nodes via a conservative mapping algorithm to ensure load preservation, while incremental displacements are returned to the fluid boundary using a profile-preserving mapping to maintain the geometric fidelity of the deformed shape.

To ensure a converged equilibrium state, the coupling loop is configured with a maximum of 20 iterations per time step. The convergence criterion is based on the Root Mean Square (RMS) change of the transferred data; the coupling loop continues until the RMS change for all data transfers drops below a target of 1×10^{-4}. This rigorous convergence check ensures that the final result represents a true balance between aerodynamic forces and structural stiffness.

6.2 Results and Discussion

The convergence behavior of the coupled simulation is illustrated in Fig. 20, which presents the root-mean-square (RMS) history of the data transfer variables. The System Coupling setup manages two primary transfers: the aerodynamic pressure and force from the fluid domain to the structure, and the structural displacement back to the fluid domain.

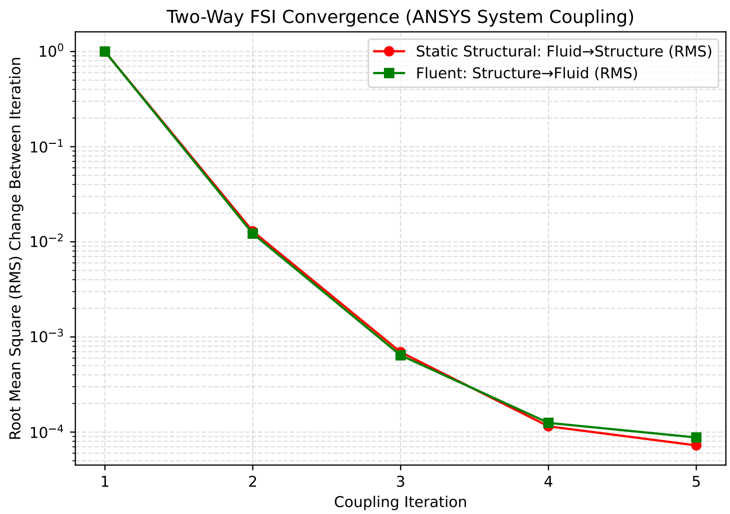

Figure 20: RMS convergence history of the data transfer variables in the two-way FSI simulation.

As observed in the figure, the coupling iterations exhibit rapid convergence. By the 5th iteration, the RMS values for both data transfers fall below the prescribed convergence criterion of 10^{-4}. This indicates that a consistent aero-structural equilibrium is established quickly within the load step, ensuring that the final reported aerodynamic loads and structural deformations represent a fully converged two-way FSI state.

A quantitative comparison between the results obtained from the one-way FSI optimization and the high-fidelity two-way FSI verification for the Best Feasible Design (DP 482) is summarized in Table 6. The comparison focuses on four key performance metrics: total drag, total lift, maximum von Mises stress, and vertical wing tip deflection. It is observed that the differences between the two approaches are relatively modest, ranging between 1% and 3% for all quantities of interest. Specifically, the aerodynamic lift and drag increase by 1.28% and 2.14% respectively in the coupled simulation. This increase is attributed to the aeroelastic deformation, where the structural deflection slightly modifies the local angle of attack and effective camber, resulting in higher integrated forces. Consequently, the structural response also intensifies, with the maximum von Mises stress increasing by 2.09% and the wing tip deflection by 2.49%. While these discrepancies are small in a global sense (suggesting that the one-way FSI provides a reasonable approximation for this stiffness-driven design), the implications for design feasibility are significant.

Table 6: Comparison between one-way and two-way FSI results for the optimized design (DP 482).

Case	Drag (N)	Lift (N)	Max von Mises (MPa)	Wing tip deflection (mm)
One-way FSI	923.07	11142	163.01	148.84
Two-way FSI	942.80	11285	166.41	152.55
Difference	2.14%	1.28%	2.09%	2.49%

Crucially, the DP 482 design violates the 150mm tip deflection constraint under realistic two-way coupled conditions. While the optimization minimized mass by pushing deflection to 148.84 mm, the resulting 1.2 mm margin was insufficient to accommodate the 2.49% increase induced by aeroelastic feedback. The final equilibrium deflection of 152.55 mm makes the design infeasible, demonstrating that relying on one-way FSI for active constraints is non-conservative without adequate safety margins. It is important to note that this analysis employs "static FSI", utilizing a Static Structural solver to find the steady-state equilibrium. A Transient Structural formulation, typically used for dynamic responses like flutter, was not required as only the final steady state was sought.

7 Conclusion

This project successfully demonstrated a comprehensive structural sizing workflow for the Piper PA-38 wing, integrating CFD, FEA, and numerical optimization. The study proceeded through three distinct phases, beginning with the identification of the "Root-clustered strong" rib configuration as the optimal internal layout for minimizing stress concentrations near the wing root.

In the structural sizing phase, an adaptive single-objective optimization based on one-way FSI was employed. The process successfully transformed an infeasible baseline into an optimized design (DP 482), achieving a 7.8% mass reduction (from 42.0 kg to 38.7 kg) while satisfying yield strength and stiffness requirements. The resulting material distribution was notably stiffness-driven, pushing the vertical tip deflection to 148.84 mm, leaving a margin of less than 1.2 mm against the constraint.

However, the critical insight of this study lies in the final aerostructural assessment. The high-fidelity two-way coupled FSI analysis revealed that the rigid-wing assumption inherent in the one-way approach is non-conservative. Aeroelastic feedback increased the aerodynamic lift by 1.28% and the structural deflection by 2.49%. Consequently, the optimized design, which appeared feasible under static loading, violated the stiffness constraint with a final deflection of 152.55 mm. This finding underscores the necessity of incorporating adequate safety margins when utilizing decoupled sizing methods or adopting fully coupled aeroelastic optimization for flexible wings. Future work should focus on implementing manufacturing constraints to smooth component thickness and embedding two-way coupling (two-way FSI) directly into the optimization loop to account for deformation-induced load changes, as described in Fig. 2b.

References

[1] Federal Aviation Administration, *"Pilot's Handbook of Aeronautical Knowledge,"* U.S. Department of Transportation, Federal Aviation Administration, Washington, DC, 2023.

[2] Liem, R. P., Kenway, G. K. W., and Martins, J. R. R. A., *"Multimission Aircraft Fuel-Burn Minimization via Multipoint Aerostructural Optimization,"* AIAA Journal, Vol. 53, No. 1, 2015, pp. 104–122. https://doi.org/10.2514/1.J052940

[3] Gray, A. C., and Martins, J. R., *"A Proposed Benchmark Model for Practical Aeroelastic Optimization of Aircraft Wings,"* AIAA SCITECH 2024 Forum, Orlando, FL, 2024. https://doi.org/10.2514/6.2024-2775

[4] https://en.wikipedia.org/wiki/Piper_PA-38_Tomahawk

[5] Federal Aviation Administration, *"Metallic materials properties development and standardization (MMPDS-10),"* Washington, DC, 2015.

[6] ANSYS, Inc. (2024). ANSYS 2024 R1. https://www.ansys.com

[7] Slaughter, W. S., *"The Linearized Theory of Elasticity,"* Birkhäuser Boston, Boston, MA, 2002. https://doi.org/10.1007/978-1-4612-0093-2

[8] Reynolds, O., *"IV. On the Dynamical Theory of Incompressible Viscous Fluids and the Determination of the Criterion,"* Philosophical Transactions of the Royal Society of London. (A.), Vol. 186, 1895, pp. 123–164. https://doi.org/10.1098/rsta.1895.0004

[9] Menter, F. R., *"Two-Equation Eddy-Viscosity Turbulence Models for Engineering Applications,"* AIAA Journal, Vol. 32, No. 8, 1994, pp. 1598–1605. https://doi.org/10.2514/3.12149

[10] Krige, D. G., *"A statistical approach to some basic mine valuation problems on the Witwatersrand,"* Journal of the Chemical, Metallurgical and Mining Society of South Africa, 52(6), 119–139.